ACSNANO

www.acsnano.org

ARTICLE

Tuning the Structure, Conductivity, and Wettability of Laser-Induced Graphene for Multiplexed Open Microfluidic Environmental Biosensing and Energy Storage Devices

Bolin Chen, Zachary T. Johnson, Delaney Sanborn, Robert G. Hjort, Nate T. Garland, Raquel R. A. Soares, Bryan Van Belle, Nathan Jared, Jingzhe Li, Dapeng Jing, Emily A. Smith, Carmen L. Gomes, and Jonathan C. Claussen*

Cite This: *ACS Nano* 2022, 16, 15–28

Read Online

ACCESS | Metrics & More | Article Recommendations | Supporting Information

ABSTRACT: The integration of microfluidics and electrochemical cells is at the forefront of emerging sensors and energy systems; however, a fabrication scheme that can create both the microfluidics and electrochemical cells in a scalable fashion is still lacking. We present a one-step, mask-free process to create, pattern, and tune laser-induced graphene (LIG) with a ubiquitous CO_2 laser. The laser parameters are adjusted to create LIG with different electrical conductivity, surface morphology, and surface wettability without the need for postchemical modification. Such definitive control over material properties enables the creation of LIG-based integrated open microfluidics and electrochemical sensors that are capable of dividing a single water sample along four multifurcating paths to three ion selective electrodes (ISEs) for potassium (K^+), nitrate (NO_3^-), and ammonium (NH_4^+) monitoring and to an enzymatic pesticide sensor for organophosphate pesticide (parathion) monitoring. The ISEs displayed near-Nernstian sensitivities and low limits of detection (LODs) ($10^{-5.01}$ M, $10^{-5.07}$ M, and $10^{-4.89}$ M for the K^+, NO_3^-, and NH_4^+ ISEs, respectively) while the pesticide sensor exhibited the lowest LOD (15.4 pM) for an electrochemical parathion sensor to date. LIG was also specifically patterned and tuned to create a high-performance electrochemical micro supercapacitor (MSC) capable of improving the power density by 2 orders of magnitude compared to a Li-based thin-film battery and the energy density by 3 orders of magnitude compared to a commercial electrolytic capacitor. Hence, this tunable fabrication approach to LIG is expected to enable a wide range of real-time, point-of-use health and environmental sensors as well as energy storage/harvesting modules.

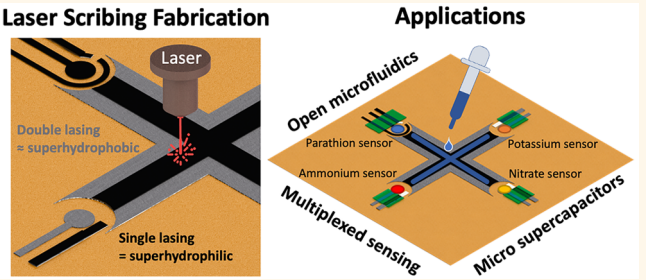

KEYWORDS: *wettability, graphene, microfluidics, laser scribing, biosensor, supercapacitor*

INTRODUCTION

Pumpless paper microfluidics have emerged as one of the most prominent tools to provide inexpensive and effective fluid transport for in-field or point-of-care sensors including those associated with disease diagnostics,[1−5] environmental monitoring,[6,7] food safety,[8] and water testing.[9] However, paper microfluidics are hindered by issues of biofouling and premature saturation which can significantly impede the sensitivity, detection limit, and accuracy of sensors as less than 50% of the total sample volume within the paper microfluidic typically reaches the detection zone.[10,11] A promising alternative to paper microfluidics is the recent development of pumpless on-surface fluid transport technologies known as open microfluidics.

Open microfluidics or open-surface microfluidics permit fluid transport across a surface not confined by four channel walls and without the need for absorption through a matrix

Received: May 17, 2021
Accepted: November 17, 2021
Published: November 23, 2021

https://doi.org/10.1021/acsnano.1c04197
ACS Nano 2022, 16, 15–28

such as cellulose.[12,13] Researchers have developed sophisticated techniques to manipulate single droplets of samples and reagents through the application of electrical fields (*i.e.*, digital microfluidics) or magnetic fields (*i.e.*, magnetic digital microfluidics) with open-surface microfluidics.[14−17] These techniques permit exquisite control over chemical reactions and biological analysis; however, they also require application of power and/or presample preparation with magnetic particles, which significantly increase operational complexity. What is needed for the majority of in-field biosensors is simply two main capabilities: (1) fluid transport to a detection zone to enable assay operation (*e.g.*, lateral flow assays used in pregnancy, allergen, and pathogen detection kits)[18,19] and (2) flow division to enable monitoring of multiple analytes from a single test sample or multiplexed sensing (*e.g.*, metabolic biomarker monitoring in urine,[20] pathogen monitoring in food samples).[21] Moreover, realizing these two sensor capabilities on a low-cost scalable platform will ensure its widescale implementation especially where cost margins are extremely low and price transmission is asymmetric in a vertical market such as in the food industry[22] and where large data mapping is needed such as with monitoring fertilizer or pesticide runoff from farm fields to watersheds.[23,24]

Researchers have begun to address the challenge of creating low-cost, pumpless open microfluidics capable of both unidirectional fluid flow and flow that is capable of dividing along multifurcating paths.[25,26] One of the more promising avenues of research in this field is the development of technologies capable of capillary-force driven fluid transport using spatial gradients of defined surface wettability.[27,28] Such microfluidics are generally created by developing narrowing, wedge-shaped hydrophilic tracks surrounded by superhydrophobic walls that permit movement of fluid along the tracks by net Laplace pressure.[29,30] These open microfluidics eliminate the need for fluid to percolate through a porous matrix as is the case with paper microfluidics, and hence significantly reduces or completely eliminates channel saturation and biofouling. Moreover, the superhydrophobic sidewalls are inherently antifouling and therefore further reduce biomolecule adsorption on the channels, which can reduce the target analyte from reaching the detection zone of the biosensor.[31,32] However, creating open microfluidics by tuning the wettability of surfaces typically requires complex and costly fabrication techniques including postchemical treatments, such as wax printing,[2,33] photolithography with UV masks,[28,34,35] chemical modification (self-assembly monolayer chemistry), deep reactive ion etching,[36,37] or brush painting of a "fluorine" containing layer.[38−40]

The 2D carbon material known as graphene holds tremendous promise in creating low-cost, scalable open microfluidics in addition to myriad electronic applications owing to its advantageous material properties such as extremely high in-plane electrical and thermal conductivity, high specific surface area, and rich surface chemistry. Conventional methods to produce graphene including chemical vapor deposition are expensive and low-yielding processes as they require high temperatures (upward of 1000 °C), vacuum chambers, and/or cleanroom processing such as metal vapor deposition of precursor metals.[41,42] However, recent methods to inkjet, aerosol, or screen print graphene flakes obtained from chemical exfoliation of bulk graphite offer a low-cost, scalable process to produce graphene circuits that exhibit a high degree of electrical conductivity (<100 Ω sq^{-1}), albeit lower than conventional graphene fabrication methods, that are useful for a variety of electronic devices.[43−46] However, these graphene fabrication methods require postprint annealing techniques such as high temperature thermal annealing (~200−400 °C),[47−49] photonic annealing,[50] and laser annealing[51,52] to carbonize ink binders such as ethyl or nitrocellulose, evaporate ink solvents, and reduce residual graphene oxide. Such multistep (*i.e.*, print and then anneal) fabrication adds to the complexity and cost of the manufacturing process. Moreover, transforming the surface wettability of graphene to hydrophobic or near superhydrophobic often requires post-treatment (spray coating, brush painting, dip coating) of a fluorine containing layer or patterning with a rapid-pulse laser[53] to achieve the desired wettability, which as a result adds to the complexity of the fabrication process.

Recently, more scalable techniques to create printed graphene open microfluidics that are capable of fluid transport and fluid division have been explored.[54] This research on graphene open microfluidics demonstrated unidirectional fluid transport and fluid division within a cross and tree pattern *via* superhydrophilic/superhydrophobic wettability patterning.[54] Indeed, this work represents a promising step forward in developing low-cost, scalable open microfluidics capable of overcoming the aforementioned hurdles associated with paper microfluidics. However, the manufacturing of these open microfluidics requires a two-step process, spin-coating graphene ink films followed by superhydrophobic patterning by scribing micron-sized grooves into the graphene with a CO_2 laser, and it remains unclear if graphene-based biosensors could be directly incorporated into these patterns.

Herein, we report a one-step, graphene-based fabrication technique that is capable of creating open microfluidics and the electrode components needed for electrochemical biosensing and energy storage modules all through a scalable CO_2 laser scribing technique. More specifically, this manuscript demonstrates how a laser scribing process can be used to convert polyimide into electrically conductive, hydrophilic graphene (*i.e.*, laser-induced graphene (LIG)) that is used for the open microfluidic fluid tracks and the circuits for subsequent electrochemical sensing. Next, a lower power double lasing process is introduced that can transform the surface wettability of the graphene to one that is near superhydrophobic and consequently is used to create the sidewalls to complete the open microfluidics. These fabrication techniques are then implemented to create an all LIG open microfluidic cross pattern that is capable of dividing a single fluid sample into four branches to four distinct, independently electrically addressable LIG biosensors. The fabricated hydrophobic/hydrophilic structure of the patterned LIG prevents uncontrolled fluid spreading and enables appropriate electrode functionalization based on application. The hydrophobic electrodes are then distinctly functionalized with ion-selective membranes for potassium (K^+), nitrate (NO_3^-), and ammonium (NH_4^+) fertilizer ion sensing and hydrophilic electrodes with an enzyme for organophosphate pesticide sensing. Such a multiplexed biosensor system demonstrates how a single river water sample can be used to monitor fertilizer and pesticide runoff from point-of-use sites such as farm fields, golf courses, and lawns into watersheds, which consequently presents a significant environmental challenge around the world by contaminating aquatic communities[55] and drinking water supplies[56] while causing harm and destruction

https://doi.org/10.1021/acsnano.1c04197
ACS Nano 2022, 16, 15−28

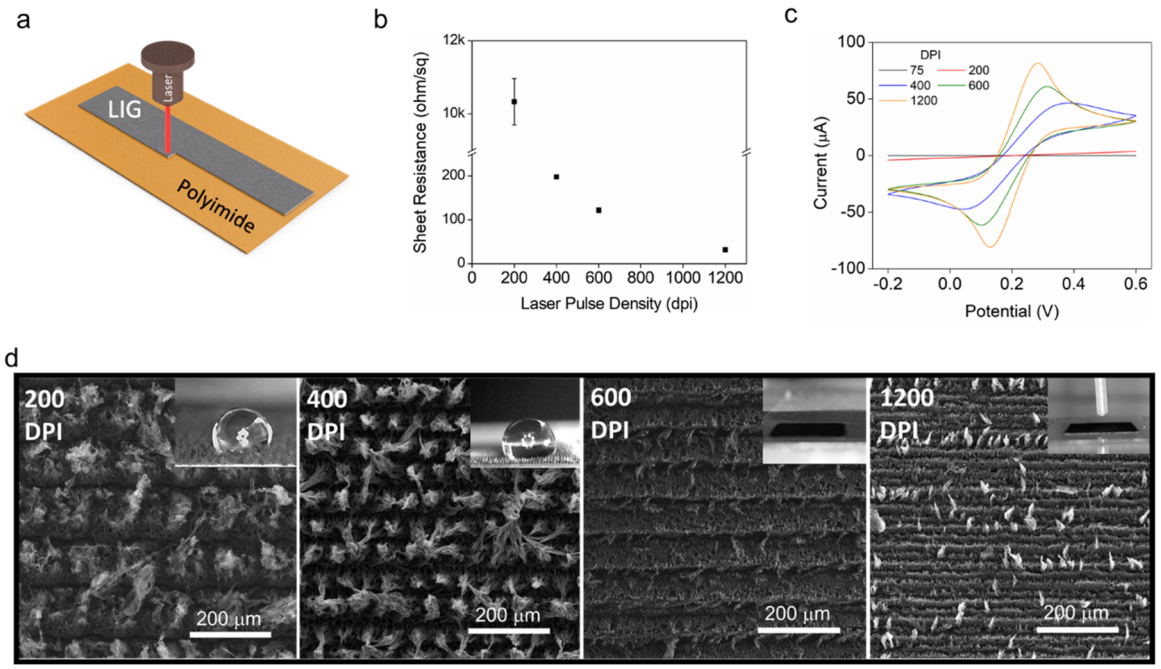

Figure 1. Fabrication scheme and the effect of laser pulse density on the electrical, electrochemical, and wetting behaviors of the laser-induced graphene (LIG). (a) Schematic of the LIG fabrication. The effect of density per inch (DPI) on the (b) sheet resistance, (c) electrochemical activity based on cyclic voltammetry curves, and (d) microstructure and surface wettability of LIG created with a single lasing (LIG-SL) shown *via* SEM imaging and water contact angle measurements, respectively. The inset of SEM images shows the single water droplet (5 μL) on the corresponding LIG surface.

to beneficial insects and mammals.[57] Finally, the improved energy density of the developed micro supercapacitors is demonstrated through the creation of LIG-based interdigitated electrodes with distinct surface wettability. This controlled tuning of the LIG wettability improves the electrode–electrolyte interface, which is important for a wide range of energy applications such as batteries, water splitting catalysts, and solar water desalination systems.

RESULTS AND DISCUSSION

Fabrication and Characterization of Laser-Induced Graphene (LIG). A CO_2 laser was used to convert polyimide substrate to laser-induced graphene (LIG), and the resultant sheet resistance of graphene was measured as the density per inch (DPI) of the laser was adjusted (200, 400, 600, and 1200 DPI) (Figure 1a,b). Figure 1b shows the sheet resistance of LIG created with a single lasing (LIG-SL) as a function of laser pulse density with speed and power fixed (15% speed; 7% power). The sheet resistance decreased greatly from over 10 kΩ sq^{-1} to less than 100 Ω sq^{-1} with increased laser pulse density. This was attributed to the overlapped lasing at high DPI as we reported previously.[58] The electrochemical reactivity of the LIG, as monitored *via* cyclic voltammetry with the ferricyanide/ferrocyanide redox probe, continued to increase as the DPI increased and the peak-to-peak potential separation continued to decrease from 331 mV to 149 mV (Figure 1c), demonstrating effective electron transfer kinetics. Next, scanning electron micrographs (SEMs) and water contact angle measurements demonstrated how variance in the DPI influenced the surface morphology and wettability of the LIG (Figure 1d). The laser trace reduces with increased DPI and results in more uniform morphology with less height difference. The continuous sheetlike LIG was formed at higher DPI (600 and 1200 DPI) in contrast of isolated fiberlike LIG formed at low DPI (less than 600 DPI). The height of LIG was also decreased from 1 mm (200 DPI) to 25 μm (1200 DPI). It should be noted here that this height is the height of the LIG pattern from the top of the graphene structures to the base of the graphene surface. The water contact angles are also reduced from 127° (hydrophobic) to 0° (superhydrophilic). Such superhydrophilicity was attributed to lasing in ambient conditions where atmospheric oxygen can more readily oxidize the edge of the LIG with increasing DPI/laser energy.[59,60]

It should be noted that a number of different techniques have been developed to create hydrophobic LIG including lasing in an inert gas chamber[59] and chemical modification of the LIG surface by forming a PDMS composite.[60] However, these methods typically require a controlled inert gas environment or the use of various chemical processes which are difficult to scale. Recently, Sodano's group reported wettability patterning of LIG by tuning the pulse density of the laser with no chemical modification.[61] However, hydrophobic LIG produced by low DPI typically suffered from high electrical resistance (300–3000 Ω sq^{-1}), sluggish electrochemical redox behavior (Figure 1b,c), and a fragile surface due to the insufficient temperature required for LIG to undergo a fiber to sheet shape conversion.[62] Hence, controlled wettability tuning of graphene with high electrical conductivity and mechanical robustness is desired for many applications including the biosensors and energy storage modules presented herein.

Here, we present a straightforward *in situ* second lasing method to create near superhydrophobic graphene. This method allows the formation of the highly conductive (15–30 Ω sq^{-1}) LIG base layer, followed by another lasing pass at lower fluence to alter the morphology of the LIG facial layer to achieve the desired electrical conductivity and surface wettability. The second lasing creates a near superhydrophobic

https://doi.org/10.1021/acsnano.1c04197
ACS Nano 2022, 16, 15–28

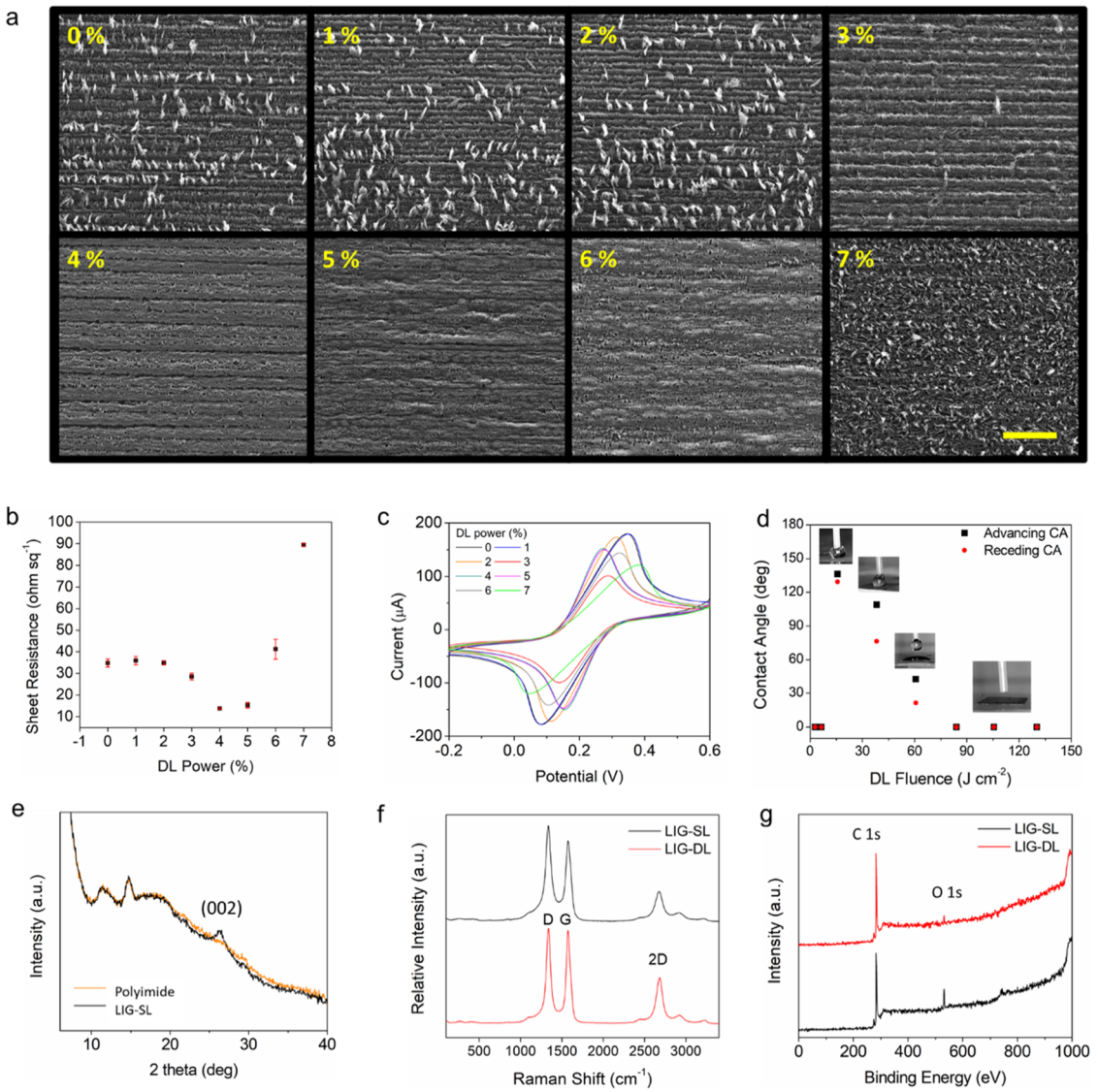

Figure 2. Characterization of LIG properties after the double lasing (DL) process: (a) the SEM images of LIG-DL created at different double lasing power (1−7%) with a 200 μm scale bar, and their corresponding (b) sheet resistance, (c) cyclic voltammetry characterization of LIG-DL samples within ferricyanide mediator solution (4 mM $Fe(CN)_6^{3-}$ and 0.1 M KCl), and (d) advancing and receding water contact angles (CA). (e) Small-angle X-ray scattering (SAXS) spectrum of polyimide (PI) and LIG-SL from single lasing (SL) at 15% speed, 7% power. (f) Raman spectra comparing LIG-SL and LIG-DL and (g) XPS survey spectra comparing LIG-SL and LIG-DL.

surface regardless of what setting was used in the first lasing, which yields more freedom of tuning the physical (structure and morphology), chemical (functional groups), and electrical (resistance) properties. Hereafter, power, speed, and fluence will be reported as percentages. Nevertheless, the relationship between percent power, speed, and fluence for the CO_2 laser is characterized with a camera and a power meter to achieve a measurable correlation between the laser settings and the actual energy that is hitting the surface of the polyimide.

To study the effect of laser power on the LIG wettability, the laser power for double lasing (DL) was varied from 1% to 7% (corresponding to 3−130 J cm^{-2}) with the rest of the parameters (speed, DPI, focal distance) unchanged. The double lasing alters the morphology of the LIG as shown in Figure 2a. Less surface protuberances are observed for DL power 3−6% samples compared to single lasing sample (0% DL power) and lower DL power samples (1−2% DL power). To clarify, high magnification images of LIG-DL created with 0% double lasing power and 7% double lasing power show the low hairlike surface perturbations at higher laser power than at lower laser power (Figure S11). The sheet resistance of the LIG-DL with various DL power were taken at ambient condition (25 °C) on a Hall effect measurement system and plotted in Figure 2b. The sheet resistance slightly decreased from 0% to 5% DL power, which could be attributed to the further reduction of LIG with the double lasing process, consequently improving electrical conductivity. However, the sheet resistance increased significantly with high DL power (7%), which could be attributed to the oxidation of LIG at high power. Moreover, these sheet resistance values represent the average readings from measurements along the lasing track and perpendicular to the lasing track. When measured separately, the sheet resistance reading perpendicular to the raster direction is about 25% higher than the parallel direction. Figure 2c shows the cyclic voltammetry response of the corresponding LIG-DLs as working electrode versus Ag/AgCl

https://doi.org/10.1021/acsnano.1c04197
ACS Nano 2022, 16, 15−28

in 0.1 M KCl containing 4 mM $K_3[Fe(CN)_6]/K_4[Fe(CN)_6]$ at a scan rate of 50 mV/s. The peak currents decreased with the increased DL power from 0% to 3%, which could be attributed to the reduced contact between electrode surface and electrolyte due to the increased hydrophobicity of LIG-DL electrodes. However, above 4% DL power, the peak currents increase again due to the improved wetting. Interestingly, the peak-to-peak separation was reduced from 271 mV (0% DL power) to 149 mV (3% DL power) with the increased hydrophobicity, which indicates an improvement in electron transfer kinetics. Laser fluence between 15.67 and 60.73 J cm^{-2} (3% and 5% DL power) leads to a change in the wettability change of the LIG surface. No change of wettability was observed on LIG-DL with a fluence less than 15.67 J cm^{-2} (2% DL power). However, the LIG-DL turns hydrophobic when the fluence is greater than 15.67 J cm^{-2}, and a laser sparking on the polyimide/LIG surface was observed during the lasing process. With the increased fluence, the hydrophobicity decreased as the contact angle reduced from 143° at 3% DL power to 21.3° at 5% DL power, and when the fluence is greater than 84 J cm^{-2} (6% DL power), the LIG-DL becomes superhydrophilic again (CA = 0°, Figure 2d insets). The contact angle hysteresis, a reflection of the activation energy required for movement of a droplet from one metastable state to another on a surface can be measured by the difference between advancing and receding contact angles.[63] For 3% DL power, hysteresis was relatively small (5.1°) compared to LIG-DL fabricated with 4% and 5% DL power (over 20°). To study the effect of fluence on the wettability of LIG, a fluence below 15.7 J cm^{-2} and above 60.7 J cm^{-2} was also applied, and no hydrophobic effect was observed. At low power, there was not sufficient energy to modify the LIG surface, and at high energy, strong oxidation is present which is similar to the LIG created by single lasing. Based on these results, we conclude that the speed 20% and power 3% is the most suitable setting for the double lasing process. Also, it should be noted these laser settings produced near superhydrophoic graphene (static water contact angle of ~143°) that is used in the subsequent open microfluidics and electrochemical sensors presented in this manuscript. The resulting near superhydrophobic graphene surface is most likely due to the reduction in superficial oxygen species and the micro/nanostructuring of the graphene surface.[54] This near superhydrophobic graphene demonstrates a high degree of water droplet repulsion even 2 weeks after electrode synthesis (Movie 1). The micro supercapacitor, which will also be presented later in this manuscript, was prepared with LIG-SL as it offers better wetting surface properties between the electrode and aqueous electrolyte and greater capacitance.

The wettability of a solid surface is strongly influenced by both the physical structure (or surface roughness) and surface chemistry. In general, the wetting of liquid on textured surfaces typically exhibit one of two states: (i) the Wenzel wetting state,[64] in which water is in full contact with the textured surface, or (ii) the Cassie–Baxter wetting state,[65] in which water is in contact with the peaks of the textured surface and air pockets are trapped in between. To further study the effect of double lasing, small-angle X-ray scattering (SAXS), Raman, and XPS analyses were conducted. From SAXS, the (002) reflection peak of graphitic crystal plane at 26.3° indicates the presence of stacked graphene layers after the lasing of polyimide (Figure 2e).[66] There was not a peak at 26.3° on the unlased polyimide sample. Raman spectroscopy obtained from LIG also supports the presence of graphene (the presence of 2D peak). Three main peaks (D, G, and 2D) are present with the D peaks at ~1350 cm^{-1} due to the defects and bending, the G peak at ~1580 cm^{-1} indicative of sp^2-bonded carbon atoms, and the 2D peak at ~2700 cm^{-1} characteristic of graphene, consequently indicating the presence of few-layered graphene (Figure 2f). The hydrophobic LIG also has the expected peak position with a slightly higher D/G ratio (1.1 ± 0.1 compared to 1.01 ± 0.07) and a lower 2D/G ratio (0.38 ± 0.05 compared to 0.51 ± 0.03) due to the further bending of the LIG surface after double lasing. The high DPI and power offer higher degrees of laser irradiation which is critical for producing highly conductive graphene. However, such high temperature lasing in ambient air allows oxygen atoms to naturally react with the carbon atoms on the graphene that creates a variety of hydrophilic oxygen-containing functional groups (*e.g.*, carboxyl, hydroxyl, and carbonyl) on the LIG surface. These oxygen-containing functional groups have an excellent affinity toward water droplets, which makes the single lasing sample superhydrophilic. This is evident from the XPS survey of LIG before and after double-lasing (Figure 2g). Higher O 1s content is observed with the single lasing sample while the oxygen content decreased from 15.85% to 4.01% after the second lasing. The increased C–C peaks, which are well-known to be hydrophobic, lead to the increased hydrophobicity of the LIG-DL. The deconvoluted peak from the C 1s spectra of the as-prepared graphene oxide is attributed to C=C/C–C bonds (284.6 eV), epoxy (C–O)/hydroxyl (C–OH) bonds at 286.6 eV, carbonyl (C=O) bonds at 287.9 eV, and carboxyl (C (=O)–OH) bonds at 289.2 eV. From C 1s spectra, the asymmetric shape of the main peak at 284.0 eV and the presence of the high binding energy pi–pi* satellite show that the C in both samples are mainly sp^2 type (Figure S2a). This is confirmed by the D parameter analysis shown in the C *KLL* spectra (Figure S2b). The separations between the maxima and minima in differentiated Auger spectra from both samples are close to that from sp^2 graphite. To further investigate such changes in hydrophobicity, cross-sectional SEM images (Figure S3) were used to study physical structure of the LIG before and after double lasing. Both methods create a porous structure with an increased film thickness, and numerous microfibers with a diameter less than 1 mm were formed by double lasing. Such microstructures at different scales lead to the increased hydrophobicity of LIG. The synergistic effect of the microstructure surface and the hydrophobic property of the surface functional groups is critical for superhydrophobicity.[54,67] The LIG-DL with 3% DL power presents hydrophobic behavior with an average static contact angle of 143° which is very close to superhydrophobic (static contact angle ≥145°)[68] without significantly affecting the electrical conductivity. We further demonstrate the impact of such wettability tuning of LIG by creating multiplexed biosensors as well as a flexible energy storage device.

Design and Fabrication of LIG-Based Multiplexed Electrochemical Biosensors with Open Microfluidics. The wettability tuning of LIG, while retaining advantageous electrical properties, make it an ideal candidate for creating low-cost open microfluidics sensing devices. Graphene-based electrochemical sensors are inherently well-suited to monitor both small ions and large chemical compounds, owing to graphene's high surface area, fast electron transport, and rich surface chemistry.[69] Laser scribing has been used to directly obtain graphene nanomaterials from different substrates for

https://doi.org/10.1021/acsnano.1c04197
ACS Nano 2022, 16, 15–28

Scheme 1. Schematic of the All in One Open-Microfluidics Multiplex Biosensing Platform Fabrication and Functionalization for Ion and Pesticide Sensing

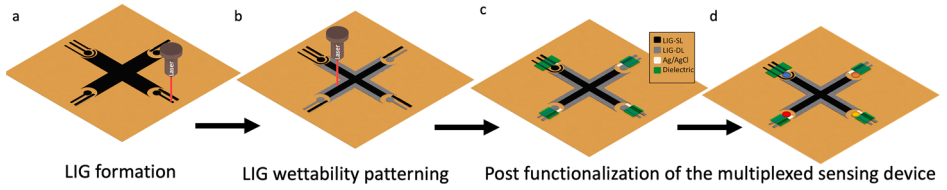

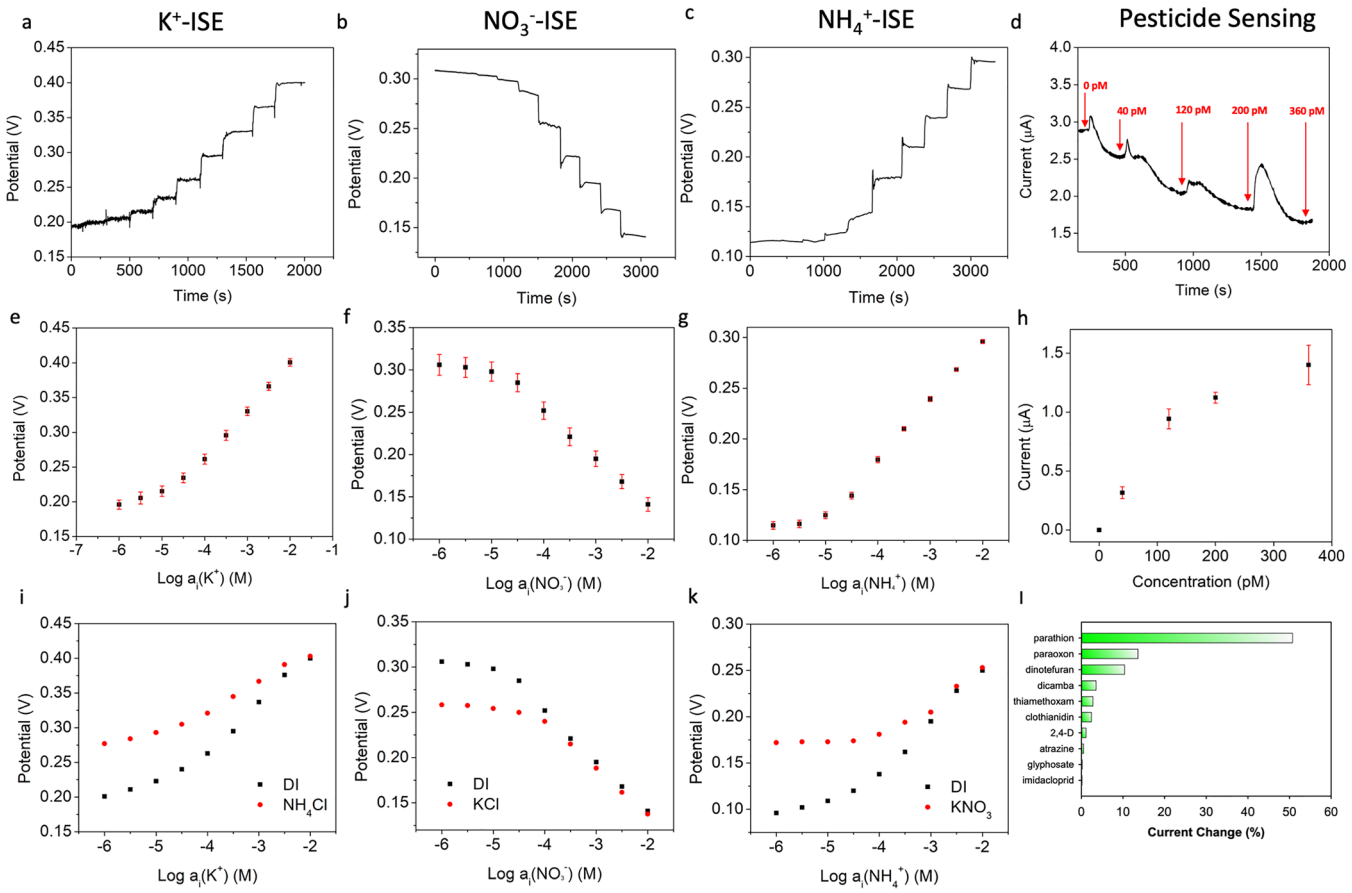

Figure 3. Open circuit potential response of the (a) potassium ion-selective electrode (K^+ ISE), (b) nitrate ion-selective electrode (NO_3^- ISE), and (c) ammonium ion-selective electrode (NH_4^+ ISE) to KCl, KNO_3, and NH_4Cl solutions, respectively, within the concentration range from 10^{-6} M to 10^{-2} M. The corresponding (e–g) calibration plots and (i–k) selectivity tests with 2 mM of fixed interference ions. Electrochemical response of the pesticide sensor. (d) The current vs time response to different concentrations of parathion, (h) corresponding calibration plot, and (l) selectivity test of acetylcholinesterase sensor comparing atrazine, dicamba, glyphosate, thiamethoxam, dinotefuran, imidacloprid, clothianidin, paraoxon, and parathion. Error bars represent the standard deviation with n = 3.

fluid transport and energy applications.[70−73] The fabrication schematics of all the key components of the multiplexed sensing device: laser induced graphene-open microfluidics (LIG-OM), laser induced graphene-ion-selective electrode (LIG-ISE), and laser induced graphene-pesticide sensor (LIG-PS) are detailed in Scheme 1a–d. The first lasing converts polyimide into superhydrophilic OM tracks as well as the electrochemical sensors. These patterns are easily created through the use of a computer aided design (CAD) file that is uploaded into a computer that controls the laser (Figure 3a). The second lasing selectively converts the boundary of OM track and electrodes for ISEs from superhydrophilic to near superhydrophobic. This step is critical for ISEs to reduce water-layer formation which consequently limits sensor drift and increases sensor longevity.[74−76] Four types of sensors are fabricated within the multiplexed sensing platform, namely, a potassium ion-selective electrode (K^+ ISE), a nitrate ion-selective electrode (NO_3^- ISE), an ammonium ion-selective electrode (NH_4^+ ISE), and an enzymatic-based pesticide sensor, while a solid-state polyvinyl butyral (PVB)-based Ag/AgCl reference electrode is used in conjunction with all of the sensors.[77] The ISEs were created by drop coating a polymetric ion-selective membrane that is distinctly selective to each of the mentioned ions onto the LIG-DL electrodes while the enzyme acetylcholinesterase (AChE) was cross-linked with glutaraldehyde and drop coated onto a LIG-SL electrode for the detection of organophosphate pesticides (parathion) (see the Experimental Section). A video demonstrates how a fluid sample (water containing green fluorophore for visualization) deposited from a pipettor divides and moves to the four

https://doi.org/10.1021/acsnano.1c04197
ACS Nano 2022, 16, 15−28

Table 1. Performance Summary of the Potassium (K^+), Nitrate (NO_3^-), and Ammonium (NH_4^+) Ion Selective Electrodes (ISEs) Fabricate Using LIG-DL[a]

ISE	sensitivity (mV/dec)	detection limit (M)	standard potential E° (mV)	selectivity coefficients	
K^+	60.87 ± 0.41	$10^{-5.01\pm0.02}$	521.40 ± 39.10	$\log K^{pot}_{i,NH_4^+}$	−1.2 ± 0.1
NO_3^-	−57.87 ± 1.43	$10^{-5.07\pm0.01}$	39.75 ± 13.14	$\log K^{pot}_{i,Cl^-}$	−2.0 ± 0.2
NH_4^+	51.66 ± 3.06	$10^{-4.89\pm0.08}$	369.50 ± 35.35	$\log K^{pot}_{i,K^+}$	−0.7 ± 0.2

[a]Values given are averages of three replicates ± standard deviations.

sensors at the ends of the open microfluidic track (Movie 2). The open circuit potential (OCP) response of the K^+ ISE, NO_3^- ISE, and NH_4^+ ISE to KCl, KNO_3, and NH_4Cl solutions, respectively, within the concentration range varying from 10^{-6} M to 10^{-2} M, were acquired in deionized water (DI) (Figure 3e−g). All ISEs show near-Nernstian behaviors with sensitivities of 60.87 mV/dec, −57.87 mV/dec, and 51.66 mV/dec for K^+, NO_3^-, and NH_4^+, respectively. The limit of detection (LOD) of each ISE is also calculated to be $10^{-5.01}$ M, $10^{-5.07}$ M, and $10^{-4.89}$ M for K^+, NO_3^-, and NH_4^+, respectively (Figure 3i−k). The high selectivity of a potentiometric sensor is a key factor to ensure the practical applications of ISEs in complex sample matrixes. For this purpose, cross interference among the selected ions was tested by using the fixed interference method (FIM) where the concentration of the target analyte ion is varied in a background of a fixed concentration (2 mM) of chosen interference (Figure 3m−o).[78] These LIG-based sensors show comparable sensitivity and selectivity to other carbon-based solid contact ISEs (Table 1).[58,69,79−81] By tuning the wettability of LIG from superhydrophilic to near superhydrophobic, the formation of a water layer was significantly suppressed, thus leading to reduced sensor to sensor variations (Figure S4). In fact, the LIG-DL nitrate ion selective sensors displayed a negligible change in the limit of detection and sensitivity after repeated weekly testing for 2 months (Figure S5). The same LIG-DL nitrate ion selective sensors also displayed a negligible change in sensitivity after 1 year in dry, ambient storage (Figure S6). It should be noted that for solid contact ion selective electrodes, water from measurement samples can migrate into the interface between the polymeric sensing layer and the transduction layer, which in this case is the developed LIG electrode.[74] This water layer then accumulates ions, reaching a new equilibrium concentration with each sample test and can lead to selectivity, stability, and drift issues in the ISE response.[82] The strain resistance of LIG-ISE fabricated as LIG-DL was performed by measuring the response of the NO_3^- ISE to KNO_3 (1 mM) under three different bending conditions, 10, 50, and 100 cycles (Figure S7).[83] The difference in potential measured in nitrate solution was evaluated before and after bending the sensors on rods with diameters of 5 mm, 10 mm, and 20 mm. The only curvature that showed a significant difference between cycles ($p = 0.003$) was the rod of 5 mm. For this rod, the sensors were disabled after 100 cycles, the most drastic condition tested. Neverthless, even for this harshest bending condition, the sensors could endure up to 50 cycles. Apart from this, all sensors exhibited consistent performance for the other curvatures, for up to 100 cycles. This test demonstrates flexibility of the sensors under harsh conditions and hence such sensors show promise for use in the field.[69,84]

For pesticide sensing, electrochemical measurements were performed on an all LIG three electrode setup (see the Experimental Section) with amperometry, which measured the signal induced by acetylthiocholine chloride (ACTH) at a working potential of 0.2 V vs Ag/AgCl, considering that higher potentials caused fouling of the electrode surface. Each sensor was tested using parathion concentrations from 40 pM to 360 pM. Results were obtained from the current−time plot for successive concentration additions, and the average response of three sensors were plotted (Figure 2h,l,p). The response yielded the parathion sensitivity as parathion irreversibly inhibited AChE in each addition, thus causing a decreased signal as the reaction between ACTH and AChE was limited. The sensor exhibited an extremely low LOD of 15.4 pM, the lowest LOD for any parathion sensor to date,[85] as well as a linear range of 40−120 pM that is similar to other carbon nanomaterial-based sensors made with graphene nanoribbons[86] (LOD, 0.5 nM; linear range, 5 nM−2780 μM), reduced graphene oxide-palladium[87] (LOD, 7.4 nM; linear range, 0.1−125 μM), and screen printed modified graphene[88] (LOD, 52 pg/L; linear range, 0.1−1000 ng/L). It is reported that small enzymatic concentrations (~200 units/mL) when sensing pesticides yields low limits of detection as well as a limited linear range.[89−91] This means that with smaller amounts of enzyme on the surface of the electrode, less pesticide is needed to fully inhibit the enzyme activity correlating to a lower linear range as compared to an inhibitory sensor with a higher enzyme concentration. The sensor was tested against 40 nM of possible interference pesticides including the commonly applied herbicides atrazine, glyphosate, dicamba, and 2,4-dichlorophenoxyacetic acid; the heavily used neonicotinoids imidacloprid, thiamethoxam, clothianidin, and dinotefuran; and finally, with paraoxon which is a metabolite of parathion. These results show that 40 nM of the target parathion yielded approximately a 50% change in current as compared to the leading interference species, paraoxon, which yielded a current change of approximately 10% (Figure 2p). This indicates that the biosensor exhibits a high affinity for parathion compared to other commonly applied pesticides and hence could be used in a wide variety of locations even within major agricultural regions where numerous pesticide types are frequently used.

Next, the multiplexed sensors were tested in a local river water sample (from South Skunk River, Ames, IA, January 2021) to evaluate sensor performance within complex biological matrixes. The OCP response to 1 mM target ion in river water and 1 mM target ion in deionized water were compared for all three ISEs. The signal obtained in river water was 104%, 98%, and 102% for the K^+, NO_3^-, and NH_4^+ ISEs as compared to the signal obtained in deionized water using the respective calibration curves (Table S1). For the pesticide sensor, an 84% signal recovery was observed in river water

https://doi.org/10.1021/acsnano.1c04197
ACS Nano 2022, 16, 15−28

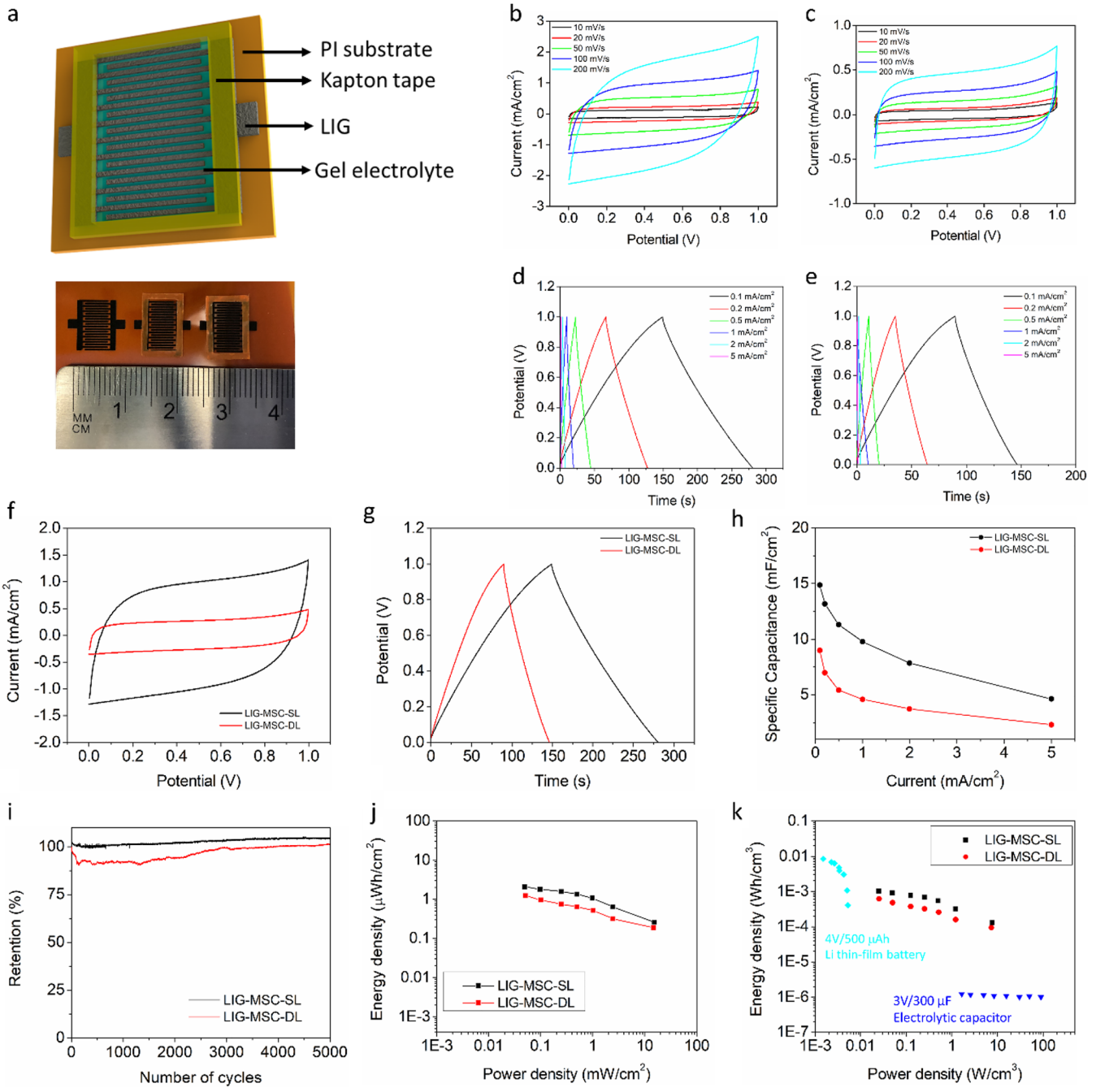

Figure 4. (a) Scheme of the laser-induced graphene micro supercapacitor (LIG-MSC) and photo of LIG-MSC-SL. (b,c) Cyclic voltammetry (CV) curves of LIG-MSC-single lasing (LIG-MSC-SL) and LIG-MSC-double lasing (LIG-MSC-DL) at scan rates of 10, 20, 50, 100, 200 mV/s. (d,e) Galvanostatic charge−discharge (GCD) curves of LIG-MSC-SL and LIG-MSC-DL at current densities of 0.1, 0.2, 0.5, 1, 2, 5 mA/cm^2. The comparison of electrochemical performance between LIG-MSC-SL and LIG-MSC-DL, (f) CV curves at a scan rate of 100 mV/s, (g) GCD curves at a current density of 1 mA/cm^2, (h) specific capacitance calculated from GCD curves, and (i) capacity retention under 5000 GCD cycles at a current density of 1 mA/cm^2. Ragone plot showing the (j) areal and (k) volumetric energy and power density of the devices.

(Figure S8). The overall sensing performance of the developed multiplexed sensors demonstrates the practical application of rapid in-field water sample tests with high accuracy compared to commercial liquid junction-based ion selective electrodes that are geared to water analysis typically in a laboratory. Moreover, the electrochemical parathion sensor overcomes the challenges associated with commercially available environmental biosensors that are geared toward rapid assessment in the field (*e.g.*, OrganaDx by MyDx). These field-based environmental sensors generally require pipetting into multiple wells for multiplexed sensing and rely upon colorimetric test results which can be easily misread under different lighting conditions, do not report concentration readings as the test gives only a yes/no result, and can be fouled/misread due to particulate matter found in field samples.[92]

Design and Fabrication of LIG-Based Micro Supercapacitors. To demonstrate the broad impact of wettability tuning in other applications, micro supercapacitors (MSC)

https://doi.org/10.1021/acsnano.1c04197
ACS Nano 2022, 16, 15−28

were prepared with superhydrophilic and near superhydrophobic LIG in interdigitated electrode (IDE) patterns (Figure 4a). Two types of laser induced graphene micro supercapacitor electrodes were fabricated: superhydrophilic LIG created by single lasing (LIG-MSC-SL) and hydrophobic LIG created by double lasing (LIG-MSC-DL). The MSC electrodes were first created by scribing the polyimide (PI) substrate with a CO_2 laser. Then, the poly(vinyl alcohol) (PVA)-based gel electrolyte containing 1 M sulfuric acid (H_2SO_4) was used to complete the fabrication of the MSC devices (see the Experimental Section). To study the effect of IDE wettability on the electrochemical performance of the MSC, LIG-SMC-SL, and LIG-MSC-DL with the same dimensions (finger size 5 mm by 2 mm, 10 pairs in total which makes for 0.2 cm^2 effective electrode area) were fabricated. Cyclic voltammetry (CV) and galvanostatic charge−discharge (GCD) experiments in a potential window from 0 to 1.0 V were performed to study the electrochemical performance. Figure 4b,c shows the CV curves of the LIG-MSC-SL and LIG-MSC-DL at different scan rates (10, 20, 50, 100, and 200 mV/s). The nearly rectangular shapes of CV curves indicate the electrical double layer formation. The GCD curves of the LIG-MSC-SL and LIG-MSC-DL (Figure 4d,e) at different current densities (0.1, 0.2, 0.5, 1, 2, 5 mA/cm^2) show triangular shapes which indicate capacitive behavior.[93,94] The LIG-MSC-SL sample shows larger area under the CV curve and GCD curve (Figure 4f,g) compared to the LIG-MSC-DL under the same scan rate and current density, indicating the higher capacitance of the superhydrophilic LIG electrodes. The near superhydrophobic LIG electrode reduces wetting compatibility between the PVA-based gel electrolyte and the LIG matrix, often resulting in pores within the electrode interior not fully wetted by the electrolyte solution. The abundant presence of −OH groups in PVA improves the wetting of electrolyte on LIG, which facilitates the ion-transport and higher accessibility to the electrode surface. The LIG-MSC-SL exhibits higher specific capacitance (C_{sp}) over a wide range of current densities from 0.1 to 5 mA/cm^2 compared to LIG-MSC-DL, with the highest C_{sp} of 14.9 mF/cm^2. Both LIG-MSC-SL and LIG-MSC-DL samples retain their capacitance even after 5000 cycles of GCD at 1 mA/cm^2. Multiple MSCs in series and parallel with different dimensions can also be prepared by simply altering the drawing files to extend the voltage windows and capacities (Figure S9a,b). Ragone plots were used to compare the LIG-MSC with commercially available electrolytic capacitor and thin-film batteries. The areal metrics are shown in Figure 4j, and volumetric metrics are shown in Figure 4k. The LIG-MSCs exhibit 2 orders of magnitude improvement of power density at similar energy densities compared to a Li-based thin-film battery and 3 orders of magnitude of improvement of the energy density compared to a commercial electrolytic capacitor.[94] Also, the LIG-MSC-SL shows slightly higher energy density (2.07 μWh/cm^2) compared to LIG-MSC-DL (1.25 μWh/cm^2) at 0.1 mA/cm^2. Lithium hexafluorophosphate solution ($LiPF_6$) in ethylene carbonate, dimethyl carbonate, and diethyl carbonate are also used as the model organic electrolytes to compare the effect of wettability on the capacitance of LIG-MSC. The specific capacitance for LIG-MSC-SL is slightly higher at 1.08 mF/cm^2 as compared to 0.81 mF/cm^2 for LIG-MSC-DL with $LiPF_6$ as the organic electrolyte based on the CV measurement (Figure S10) at a scan rate of 50 mV/s. Such controlled wettability tuning of LIG allows easy tuning of the electrode surface based on the property of the electrolyte. For example, organic electrolytes used in energy storage devices require a hydrophobic electrode for sufficient wetting contact and ion transport.[95] In this case, LIG-DL can be easily fabricated by simply adding one more lasing pass.

CONCLUSION

A simple and sensitive multiplexed electrochemical sensor combined with open microfluidics was developed for environmental sensing applications by controlling the wettability of LIG. The open microfluidics enabled rapid sampling and required less volume of sample solution compared to conventional laboratory-based electrochemical sensing. The ion-selective electrodes were capable of detecting K^+, NO_3^-, and NH_4^+ ions down to the micromolar range in the lab and millimolar range in river water samples. The pesticide sensor successfully detected parathion and exhibited a LOD of 15.4 pM, which is the lowest LOD for any electrochemical parathion sensor to date. Such LIG based microfluidics sensing platforms are highly scalable as the graphene electrodes can be simply manufactured through a direct write laser process performed in ambient conditions with a ubiquitous CO_2 laser while graphene functionalization could be carried out with automated pipettor systems. Using the same LIG fabrication technique, an electrochemical micro supercapacitor (MSC) was developed. The LIG-based MSC exhibited a high power density that was 2 orders of magnitude greater than a Li-based thin-film battery, and the energy density was 3 orders of magnitude greater than compared to a commercial electrolytic capacitor.

Moreover, this manuscript demonstrates a method to control the surface wettability of the LIG from highly hydrophobic to hydrophilic by only changing the lasing parameters. This lasing is also done in ambient conditions without the need for lasing in an oxygen limited environment such as within a nitrogen or argon filled chamber; hence, the controlled surface wettability patterning with the direct write laser demonstrated herein is highly scalable. Controlling the surface wettability of graphene can significantly improve the performance of electronics associated with electrochemical sensing,[74,96−99] energy storage,[100−102] and solar water desalination in addition to permitting open fluidic fluid transport.[103] More specifically, superhydrophilic graphene with contact angles below 10° has proven important to many applications including as a wicking material in heat pipes, enhanced boiling heat transfer,[104,105] and solar thermal water desalination.[106−108] Superhydrophobic graphene promotes the development of self-cleaning[109] and anti-icing[110,111] surfaces. Smart LIG surfaces created by facile surface wettability could lead to low-cost microfluidics as well as benefiting broader applications that involve interface chemistry such as electrochemical sensing, energy storage, and oil/water separation. Hence, this tunable fabrication approach of LIG is expected to enable real-time, point-of-use health, and environmental monitoring across a wide range of applications including sensors, biosensors, wearables, antennas, energy harvesters, energy storage modules, and single-use electronics.

EXPERIMENTAL SECTION

Materials and Reagents. Polyvinyl chloride, 2-nitrophenyl octyl ether, tridodecylmethylammonium nitrate, tetrahydrofuran, potassium nitrate, nonactin, potassium tetrakis(4-chlorophenyl)borate, ammonium chloride, valinomycin, and potassium chloride were purchased

https://doi.org/10.1021/acsnano.1c04197
ACS Nano 2022, 16, 15−28

from Sigma-Aldrich. Polyimide film (125 μm thick) was purchased from DuPont. Silver/silver chloride paste (Cl-4001) was purchased from EMS. Acetylcholinesterase (AChE) from *Electrophorus electricus* (lyophilized powder, 200−1000 units/mg), parathion, atrazine, dicamba, glyphosate, thiamethoxam, dinotefuran, imidacloprid, clothianidin, paraoxon were purchased from Sigma-Aldrich and all other pesticide sensing materials unless otherwise specified. Deionized (DI) water was used after passing through a B-pure water purification system (18.2 MΩ cm^{-2}).

Fabrication and Characterization of the LIG. The LIG electrodes were created by lasing a polyimide (PI) film with a 75 W CO_2 laser (Epilog Fusion M2) that has a spot size of approximately 76 μm. The laser setting for creating LIG-SL is speed 15%, power 7%, dot per inch (DPI) 1200 unless specified. The laser setting for creating LIG-DL is speed 20%, power 3%, dot per inch (DPI) 1200 unless specified. LIG-ISE sensors were created with the combination of LIG-SL and LIG-DL settings. LIG-PS sensors were created with the LIG-SL setting. A two-electrode array for ISE sensors and a three-electrode array for enzymatic sensors and interdigitated electrodes for supercapacitors were simultaneously prepared. Laser power and energy was measured by a thermal sensor from Ophir (model no. F150A-BB-26-PPS) with a StarLite Meter. Sheet resistance was measured by Hall measurement systems (MMR H5000) at room temperature. The sheet resistance was measured by the Van der Pauw method with a square sample and electrical contact at the four corners. The contact angle of water was measured using a goniometer with an automated dispensing system (Rame-Hart p/n 100-22) for droplet dispensing. ImageJ was used to process contact angle image and estimate the contact angle value. Raman spectroscopy were performed using an XploRA PLUS confocal Raman upright microscope equipped with a 532 nm excitation source and a synapse electron multiplying charge coupled device camera (Horiba Scientific, NJ, USA). The intensity was determined for the D, G, and 2D bands by fitting the data to a Lorentzian function. Scanning electron microscopy (SEM) images were taken by an FEI Quanta 250 FEG scanning electron microscope at a 10 kV accelerating voltage. Small-angle X-ray scattering (SAXS) was performed using a XENOCS Xeuss 2.0. The Cu tube is operated at 50 kV and 0.6 mA.

Functionalization of ISE and Enzymatic Sensors. After graphene electrodes were scribed, silver/silver chloride (Ag/AgCl) paste was screen-printed onto one electrode followed by adding a PVB membrane to function as a solid-state reference electrode for both ISE and enzymatic sensors. Untreated LIG is used as a counter electrode in the case of the three-electrode array. The working electrodes for ISEs were prepared by drop-casting polymer membrane solutions onto the hydrophobic LIG (LIG-DL) working area. The NH_4^+ ion-selective membrane was prepared by drop-casting 10 mL of a mixture of ammonium ionophore I (0.4 wt %), potassium tetrakis(4-chlorophenyl)borate (0.2 wt %), 2-nitrophenyl octyl ether (69 wt %), and poly(vinyl chloride) high molecular weight (30.4 wt %) in tetrahydrofuran (THF). The NO_3^- ion-selective membrane was prepared by drop-casting 20 mL of a mixture of tridodecylmethylammonium nitrate (0.2 wt %), 2-nitrophenyl octyl ether (69 wt %), and poly(vinyl chloride) high molecular weight (30.8 wt %) in THF. The K^+ ion-selective membrane was prepared by drop-casting 20 mL of a mixture of valinomycin (0.5 wt %), dioctyl sebacate (69 wt %), and poly(vinyl chloride) high molecular weight (30.5 wt %) in THF. A solid-state reference electrode was made by depositing a membrane cocktail (10 wt % polyvinyl butyral (PVB) dissolved in methanol with saturated NaCl) onto the LIG-DL.[77]

For enzymatic sensors, an enzymatic solution was prepared by first making 10 wt % glycerol in 20 mM phosphate buffer saline (PBS). This solution was used to prepare 5 wt % bovine serum albumin (BSA). The BSA solution was used to prepare 200 units/mL of AChE. The enzyme solution was aliquoted and stored at −18 °C when not in use. Sensors were fabricated by mixing 200 units/mL with 2.5% glutaraldehyde in a 1:1 volumetric ratio and drop coating 2 μL of this solution onto the LIG (LIG-SL).

Electrochemical Sensing of ISE and Enzymatic Sensors. To test the ISEs, the electrochemical sensing experiments were performed using a PalmSens 4 electrochemical potentiostat with a multiplexer (MU8-R2). Cyclic voltammetry (CV) was performed in 0.1 M KCl with 4 mM $[Fe(CN)_6]^{4-}$ as a redox probe. The potentiostat was operated in the "open circuit potentiometry" mode. The selectivity coefficient is derived from the response of ISEs by using the fixed interference method (FIM).[112] The calibration curves of the primary ion and the respective calibration curves when the interference ion is present were measured. The primary ion activity a_i and the interfering ion activity a_j is used to calculate the selectivity coefficient using eq 1. The concentration range of the solutions was from 10^{-6} mol/L to 10^{-2} mol/L for each of the ions, ammonium, potassium, and nitrate. The range refers to the typical ammonium, potassium, and nitrate found in soil and surface water.

The corresponding selectivity coefficient is calculated with the following eq 1:

$$K_{ij}^{\text{pot}} = a_i / a_j^{z_i/z_j} \tag{1}$$

For enzymatic sensors, electrochemical sensing experiments were performed using a CH instrument potentiostat (600E series). Amperometric methods were used in detecting parathion. A working potential of 0.2 V vs Ag/AgCl was selected as a practical working potential, considering that higher potentials caused fouling of the electrode surface. The concentration range for parathion calibration was from 40 pmol/L to 360 pmol/L.

Fabrication and Characterization of Supercapacitors. Two types of laser induced graphene micro supercapacitor electrodes were fabricated: superhydrophilic LIG created by single lasing (LIG-MSC-SL) and hydrophobic LIG created by double lasing (LIG-MSC-DL). Poly(vinyl alcohol)-based (PVA) gel electrolyte was prepared by mixing 10 g of PVA powder (Mowiol 18-88, Sigma-Aldrich) into 10 mL of 1 M sulfuric acid and stirred on hot plate at 85 °C until the mixture became a clear and gluelike gel. Polyimide tape were applied to insulate the leg region of the MSC and confine the area for electrolyte. About 15 μL of the prepared gel electrolyte was applied on the finger region of the MSC. The electrochemical performance of the fabricated MSCs was characterized by galvanostatic charge−discharge (GCD), cyclic voltammetry (CV), and electrochemical impedance spectroscopy (EIS) with a Gamry Reference 3000 electrochemical station. The areal specific capacitances (C_{sp}) of each device at different current densities were calculated from the discharge curves obtained from GCD tests using eq 2:

$$C_{sp} = \frac{I}{S\frac{\Delta U}{\Delta t}} \tag{2}$$

where I is the applied discharge current (amp), A (cm^2) is the active area of the electrode (finger dimension 5 mm × 0.2 mm, 10 pairs in total which makes the effective electrode area equal to 0.2 cm^2), Δt is discharge time (second), and ΔU (volt) is the discharge voltage after the iR (current × resistance) drop is removed.

The areal energy density (Wh cm^{-3}) of each device is calculated using eq 3:

$$E = \frac{0.5 \times C_{sp} \times \Delta U^2}{3600} \tag{3}$$

The volumetric power density (W cm^{-3}) of the device is calculated from eq 4:

$$P = \frac{E}{\Delta t} \times 3600 \tag{4}$$

Data Analysis. A completely randomized design was used in this study, and the results are reported as mean ± standard deviation. Results were obtained by performing at least three independent experiments. Data analysis was performed using JMP Pro statistical software (version 15, SAS, Cary, NC).

https://doi.org/10.1021/acsnano.1c04197
ACS Nano 2022, 16, 15−28

ASSOCIATED CONTENT

Supporting Information

The Supporting Information is available free of charge at https://pubs.acs.org/doi/10.1021/acsnano.1c04197.

Fluid transport through the LIG-OM (Figure S1); XPS spectra of C 1s and differentiated C *KLL* Auger regions (Figure S2); effect of double lasing including the cross-sectional SEM images of LIG-DL created at different double lasing power (Figure S3); improved sensitivity consistency of nitrate ISEs created with LIG-DL as opposed to those with LIG-SL (Figure S4); consistent detection limit and sensitivity measurements of the LIG-DL nitrate ISEs over weekly testing for 2 months (Figure S5); shelf life data displaying nitrate LIG-DL ISE calibration plot after 1 year of dry, ambient storage (Figure S6); long-term stability of the LIG nitrate sensor (Figure S5); strain resistance of the LIG sensors against bending (Figure S7); calibration plot for the pesticide sensor used in the river water test (Figure S8); performance of ISEs in river water sample (Table S1); electrochemical performance of the LIG-MSC in series/parallel configurations (Figure S9) and with organic electrolyte (Figure S10); and high-resolution images of LIG-DL created with different lasing powers (Figure S11) (PDF)

Video showing water droplet repulsion of the LIG-DL 2 weeks after synthesis (Movie 1) (MOV)

Video showing water dividing from a pipettor along the open microfluidic tracks to the four distinct sensors (Movie 2) (MOV)

AUTHOR INFORMATION

Corresponding Author

Jonathan C. Claussen − *Department of Mechanical Engineering, Iowa State University, Ames, Iowa 50011, United States;* orcid.org/0000-0001-7065-1077; Email: jcclauss@iastate.edu

Authors

Bolin Chen − *Department of Mechanical Engineering, Iowa State University, Ames, Iowa 50011, United States*

Zachary T. Johnson − *Department of Mechanical Engineering, Iowa State University, Ames, Iowa 50011, United States*

Delaney Sanborn − *Department of Mechanical Engineering, Iowa State University, Ames, Iowa 50011, United States*

Robert G. Hjort − *Department of Mechanical Engineering, Iowa State University, Ames, Iowa 50011, United States;* orcid.org/0000-0003-2400-0710

Nate T. Garland − *Department of Mechanical Engineering, Iowa State University, Ames, Iowa 50011, United States*

Raquel R. A. Soares − *Department of Mechanical Engineering, Iowa State University, Ames, Iowa 50011, United States*

Bryan Van Belle − *Department of Mechanical Engineering, Iowa State University, Ames, Iowa 50011, United States*

Nathan Jared − *Department of Mechanical Engineering, Iowa State University, Ames, Iowa 50011, United States*

Jingzhe Li − *Department of Chemistry, Iowa State University, Ames, Iowa 50011, United States; U.S. Department of Energy, The Ames Laboratory, Ames, Iowa 50011, United States;* orcid.org/0000-0002-1856-1477

Dapeng Jing − *U.S. Department of Energy, The Ames Laboratory, Ames, Iowa 50011, United States;* orcid.org/0000-0001-7600-7071

Emily A. Smith − *Department of Chemistry, Iowa State University, Ames, Iowa 50011, United States; U.S. Department of Energy, The Ames Laboratory, Ames, Iowa 50011, United States;* orcid.org/0000-0001-7438-7808

Carmen L. Gomes − *Department of Mechanical Engineering, Iowa State University, Ames, Iowa 50011, United States;* orcid.org/0000-0003-0095-6478

Complete contact information is available at: https://pubs.acs.org/10.1021/acsnano.1c04197

Notes

The authors declare no competing financial interest.

ACKNOWLEDGMENTS

The authors gratefully acknowledge funding support from the National Science Foundation under Award Numbers ECCS-1841649 and CMMI-2037026 and CBET-1706994, CBET-1756999, and CBET-1805512, from the National Institutes of Health under award number 1U01AA029328-0, as well as from the National Institute of Food and Agriculture, U.S. Department of Agriculture, under Award Number 2020-67021-31375, 2021-67021-34457, and 2021-67011-35130. The authors wish to acknowledge the Materials Analysis and Research Laboratory (MARL) staff at Iowa State University for the support and help with the SEM, XPS, and SAXS experiments.

REFERENCES

(1) Martinez, A. W.; Phillips, S. T.; Whitesides, G. M.; Carrilho, E. Diagnostics for the Developing World: Microfluidic Paper-Based Analytical Devices. *Anal. Chem.* **2010**, *82* (1), 3−10.

(2) Nie, Z.; Nijhuis, C. A.; Gong, J.; Chen, X.; Kumachev, A.; Martinez, A. W.; Narovlyansky, M.; Whitesides, G. M. Electrochemical Sensing in Paper-Based Microfluidic Devices. *Lab Chip* **2010**, *10* (4), 477−483.

(3) Figueredo, F.; Garcia, P. T.; Cortón, E.; Coltro, W. K. T. Enhanced Analytical Performance of Paper Microfluidic Devices by Using Fe 3 O 4 Nanoparticles, MWCNT, and Graphene Oxide. *ACS Appl. Mater. Interfaces* **2016**, *8* (1), 11−15.

(4) Hiltunen, J.; Liedert, C.; Hiltunen, M.; Huttunen, O. H.; Hiitola-Keinänen, J.; Aikio, S.; Harjanne, M.; Kurkinen, M.; Hakalahti, L.; Lee, L. P. Roll-to-Roll Fabrication of Integrated PDMS-Paper Microfluidics for Nucleic Acid Amplification. *Lab Chip* **2018**, *18* (11), 1552−1559.

(5) Ma, J.; Yan, S.; Miao, C.; Li, L.; Shi, W.; Liu, X.; Luo, Y.; Liu, T.; Lin, B.; Wu, W.; Lu, Y. Paper Microfluidics for Cell Analysis. *Adv. Healthcare Mater.* **2019**, *8* (1), 1801084.

(6) Kung, C.-T.; Hou, C.-Y.; Wang, Y.-N.; Fu, L.-M. Microfluidic Paper-Based Analytical Devices for Environmental Analysis of Soil, Air, Ecology and River Water. *Sens. Actuators, B* **2019**, *301*, 126855.

(7) Kong, Q.; Wang, Y.; Zhang, L.; Ge, S.; Yu, J. A Novel Microfluidic Paper-Based Colorimetric Sensor Based on Molecularly Imprinted Polymer Membranes for Highly Selective and Sensitive Detection of Bisphenol A. *Sens. Actuators, B* **2017**, *243*, 130.

(8) Ma, L.; Nilghaz, A.; Choi, J. R.; Liu, X.; Lu, X. Rapid Detection of Clenbuterol in Milk Using Microfluidic Paper-Based ELISA. *Food Chem.* **2018**, *246*, 437−441.

(9) Almeida, M. I. G. S.; Jayawardane, B. M.; Kolev, S. D.; McKelvie, I. D. Developments of Microfluidic Paper-Based Analytical Devices (MPADs) for Water Analysis: A Review. *Talanta* **2018**, *177*, 176.

(10) Zhu, Y.; Xu, X.; Brault, N. D.; Keefe, A. J.; Han, X.; Deng, Y.; Xu, J.; Yu, Q.; Jiang, S. Cellulose Paper Sensors Modified with

Zwitterionic Poly(carboxybetaine) for Sensing and Detection in Complex Media. *Anal. Chem.* **2014**, *86* (6), 2871−2875.
(11) Li, X.; Ballerini, D. R.; Shen, W. A Perspective on Paper-Based Microfluidics: Current Status and Future Trends. *Biomicrofluidics* **2012**, *6* (1), No. 011301.
(12) Berthier, J.; Brakke, K. A.; Berthier, E. Introduction. *Open Microfluidics*, 1st ed.; Wiley: Hoboken, NJ, 2016; pp 1−11.
(13) Convery, N.; Gadegaard, N. 30 Years of Microfluidics. *Micro and Nano Engineering.* **2019**, *2*, 76−91.
(14) Abdelgawad, M.; Wheeler, A. R. Low-Cost, Rapid-Prototyping of Digital Microfluidics Devices. *Microfluid. Nanofluid.* **2008**, *4* (4), 349−355.
(15) Abdelgawad, M.; Wheeler, A. R. The Digital Revolution: A New Paradigm for Microfluidics. *Adv. Mater.* **2009**, *21* (8), 920−925.
(16) Zhang, Y.; Nguyen, N.-T. Magnetic Digital Microfluidics − A Review. *Lab Chip* **2017**, *17* (6), 994−1008.
(17) Samiei, E.; Tabrizian, M.; Hoorfar, M. A Review of Digital Microfluidics as Portable Platforms for Lab-on a-Chip Applications. *Lab Chip* **2016**, *16*, 2376.
(18) Jiang, N.; Ahmed, R.; Damayantharan, M.; Ünal, B.; Butt, H.; Yetisen, A. K. Lateral and Vertical Flow Assays for Point-of-Care Diagnostics. *Adv. Healthcare Mater.* **2019**, *8*, 1900244.
(19) Nguyen, V. T.; Song, S.; Park, S.; Joo, C. Recent Advances in High-Sensitivity Detection Methods for Paper-Based Lateral-Flow Assay. *Biosens. Bioelectron.* **2020**, *152*, 112015.
(20) Zhao, C.; Thuo, M. M.; Liu, X. A Microfluidic Paper-Based Electrochemical Biosensor Array for Multiplexed Detection of Metabolic Biomarkers. *Sci. Technol. Adv. Mater.* **2013**, *14*, 054402.
(21) Gehring, A. G.; Tu, S. I. High-Throughput Biosensors for Multiplexed Food-Borne Pathogen Detection. *Annu. Rev. Anal. Chem.* **2011**, *4*, 151.
(22) Lloyd, T. Forty Years of Price Transmission Research in the Food Industry: Insights. *Challenges and Prospects. J. Agric. Econ.* **2017**, *68*, 3.
(23) Carey, R. O.; Wollheim, W. M.; Mulukutla, G. K.; Mineau, M. M. Characterizing Storm-Event Nitrate Fluxes in a Fifth Order Suburbanizing Watershed Using *In Situ* Sensors. *Environ. Sci. Technol.* **2014**, *48* (14), 7756−7765.
(24) Macary, F.; Morin, S.; Probst, J. L.; Saudubray, F. A Multi-Scale Method to Assess Pesticide Contamination Risks in Agricultural Watersheds. *Ecol. Indic.* **2014**, *36*, 624.
(25) Berthier, E.; Dostie, A. M.; Lee, U. N.; Berthier, J.; Theberge, A. B. Open Microfluidic Capillary Systems. *Anal. Chem.* **2019**, *91*, 8739.
(26) Gong, M. M.; Sinton, D. Turning the Page: Advancing Paper-Based Microfluidics for Broad Diagnostic Application. *Chem. Rev.* **2017**, *117*, 8447.
(27) Temiz, Y.; Lovchik, R. D.; Kaigala, G. V.; Delamarche, E. Lab-on-a-Chip Devices: How to Close and Plug the Lab? *Microelectron. Eng.* **2015**, *132*, 156−175.
(28) Ghosh, A.; Ganguly, R.; Schutzius, T. M.; Megaridis, C. M. Wettability Patterning for High-Rate, Pumpless Fluid Transport on Open. *Lab Chip* **2014**, *14* (9), 1538−1550.
(29) Nakashima, Y.; Nakanishi, Y.; Yasuda, T. Automatic Droplet Transportation on a Plastic Microfluidic Device Having Wettability Gradient Surface. *Rev. Sci. Instrum.* **2015**, *86* (1), No. 015001.
(30) Khoo, H. S.; Tseng, F.-G. Spontaneous High-Speed Transport of Subnanoliter Water Droplet on Gradient Nanotextured Surfaces. *Appl. Phys. Lett.* **2009**, *95* (6), No. 063108.
(31) Shirtcliffe, N. J.; Roach, P. *Methods Mol. Biol.* **2013**, *949*, 269−281.
(32) Koc, Y.; de Mello, A. J.; McHale, G.; Newton, M. I.; Roach, P.; Shirtcliffe, N. J. Nano-Scale Superhydrophobicity: Suppression of Protein Adsorption and Promotion of Flow-Induced Detachment. *Lab Chip* **2008**, *8* (4), 582.
(33) Dungchai, W.; Chailapakul, O.; Henry, C. S. Electrochemical Detection for Paper-Based Microfluidics. *Anal. Chem.* **2009**, *81* (14), 5821−5826.
(34) Nakajima, A.; Nakagawa, Y.; Furuta, T.; Sakai, M.; Isobe, T.; Matsushita, S. Sliding of Water Droplets on Smooth Hydrophobic Silane Coatings with Regular Triangle Hydrophilic Regions. *Langmuir* **2013**, *29* (29), 9269−9275.
(35) Alheshibri, M. H.; Rogers, N. G.; Sommers, A. D.; Eid, K. F. Spontaneous Movement of Water Droplets on Patterned Cu and Al Surfaces with Wedge-Shaped Gradients. *Appl. Phys. Lett.* **2013**, *102* (17), 174103.
(36) Jokinen, V.; Sainiemi, L.; Franssila, S. Complex Droplets on Chemically Modified Silicon Nanograss. *Adv. Mater.* **2008**, *20* (18), 3453−3456.
(37) Jokinen, V.; Kostiainen, R.; Sikanen, T. Multiphase Designer Droplets for Liquid-Liquid Extraction. *Adv. Mater.* **2012**, *24* (46), 6240−6243.
(38) Manoudis, P. N.; Karapanagiotis, I. Modification of the Wettability of Polymer Surfaces Using Nanoparticles. *Prog. Org. Coat.* **2014**, *77* (2), 331−338.
(39) Hsu, C.-C.; Chen, P.-H. Surface Wettability Effects on Critical Heat Flux of Boiling Heat Transfer Using Nanoparticle Coatings. *Int. J. Heat Mass Transfer* **2012**, *55* (13−14), 3713−3719.
(40) Baidya, A.; Ganayee, M. A.; Jakka Ravindran, S.; Tam, K. C.; Das, S. K.; Ras, R. H. A.; Pradeep, T. Organic Solvent-Free Fabrication of Durable and Multifunctional Superhydrophobic Paper from Waterborne Fluorinated Cellulose Nanofiber Building Blocks. *ACS Nano* **2017**, *11* (11), 11091−11099.
(41) Zhang, Y.; Zhang, L.; Zhou, C. Review of Chemical Vapor Deposition of Graphene and Related Applications. *Acc. Chem. Res.* **2013**, *46* (10), 2329−2339.
(42) Claussen, J. C.; Kumar, A.; Jaroch, D. B.; Khawaja, M. H.; Hibbard, A. B.; Porterfield, D. M.; Fisher, T. S. Nanostructuring Platinum Nanoparticles on Multilayered Graphene Petal Nanosheets for Electrochemical Biosensing. *Adv. Funct. Mater.* **2012**, *22* (16), 3399−3405.
(43) Parate, K.; Pola, C. C.; Rangnekar, S. V.; Mendivelso-Perez, D. L.; Smith, E. A.; Hersam, M. C.; Gomes, C. L.; Claussen, J. C. Aerosol-Jet-Printed Graphene Electrochemical Histamine Sensors for Food Safety Monitoring. *2D Mater.* **2020**, *7*, 034002.
(44) He, Q.; Das, S. R.; Garland, N. T.; Jing, D.; Hondred, J. A.; Cargill, A. A.; Ding, S.; Karunakaran, C.; Claussen, J. C. Enabling Inkjet Printed Graphene for Ion Selective Electrodes with Postprint Thermal Annealing. *ACS Appl. Mater. Interfaces* **2017**, *9* (14), 12719−12727.
(45) Le, L. T.; Ervin, M. H.; Qiu, H.; Fuchs, B. E.; Lee, W. Y. Graphene Supercapacitor Electrodes Fabricated by Inkjet Printing and Thermal Reduction of Graphene Oxide. *Electrochem. Commun.* **2011**, *13*, 355.
(46) Randviir, E. P.; Brownson, D. A. C.; Metters, J. P.; Kadara, R. O.; Banks, C. E. The Fabrication, Characterisation and Electrochemical Investigation of Screen-Printed Graphene Electrodes. *Phys. Chem. Chem. Phys.* **2014**, *16*, 4598.
(47) Torrisi, F.; Hasan, T.; Wu, W.; Sun, Z.; Lombardo, A.; Kulmala, T. S.; Hsieh, G.-W.; Jung, S.; Bonaccorso, F.; Paul, P. J.; Chu, D.; Ferrari, A. C. Inkjet-Printed Graphene Electronics. *ACS Nano* **2012**, *6* (4), 2992−3006.
(48) Secor, E. B.; Prabhumirashi, P. L.; Puntambekar, K.; Geier, M. L.; Hersam, M. C. Inkjet Printing of High Conductivity, Flexible Graphene Patterns. *J. Phys. Chem. Lett.* **2013**, *4* (8), 1347−1351.
(49) Secor, E. B.; Gao, T. Z.; Islam, A. E.; Rao, R.; Wallace, S. G.; Zhu, J.; Putz, K. W.; Maruyama, B.; Hersam, M. C. Enhanced Conductivity, Adhesion, and Environmental Stability of Printed Graphene Inks with Nitrocellulose. *Chem. Mater.* **2017**, *29*, 2332.
(50) Secor, E. B.; Ahn, B. Y.; Gao, T. Z.; Lewis, J. A.; Hersam, M. C. Rapid and Versatile Photonic Annealing of Graphene Inks for Flexible Printed Electronics. *Adv. Mater.* **2015**, *27* (42), 6683−6688.
(51) Das, S. R.; Nian, Q.; Cargill, A. A.; Hondred, J. A.; Ding, S.; Saei, M.; Cheng, G. J.; Claussen, J. C. 3D Nanostructured Inkjet Printed Graphene *via* UV-Pulsed Laser Irradiation Enables Paper-Based Electronics and Electrochemical Devices. *Nanoscale* **2016**, *8* (35), 15870−15879.

https://doi.org/10.1021/acsnano.1c04197
ACS Nano 2022, 16, 15−28

(52) Hondred, J. A.; Stromberg, L. R.; Mosher, C. L.; Claussen, J. C. High-Resolution Graphene Films for Electrochemical Sensing *via* Inkjet Maskless Lithography. *ACS Nano* **2017**, *11* (10), 9836−9845.
(53) Das, S. R.; Srinivasan, S.; Stromberg, L. R.; He, Q.; Garland, N.; Straszheim, W. E.; Ajayan, P. M.; Balasubramanian, G.; Claussen, J. C. Superhydrophobic Inkjet Printed Flexible Graphene Circuits *via* Direct-Pulsed Laser Writing. *Nanoscale* **2017**, *9* (48), 19058−19065.
(54) Hall, L. S.; Hwang, D.; Chen, B.; Van Belle, B.; Johnson, Z. T.; Hondred, J. A.; Gomes, C. L.; Bartlett, M. D.; Claussen, J. C. All-Graphene-Based Open Fluidics for Pumpless, Small-Scale Fluid Transport *via* Laser-Controlled Wettability Patterning. *Nanoscale Horizons* **2021**, *6* (1), 24−32.
(55) Graymore, M.; Stagnitti, F.; Allinson, G. Impacts of Atrazine in Aquatic Ecosystems. *Environ. Int.* **2001**, *26* (7−8), 483−495.
(56) Mekonen, S.; Argaw, R.; Simanesew, A.; Houbraken, M.; Senaeve, D.; Ambelu, A.; Spanoghe, P. Pesticide Residues in Drinking Water and Associated Risk to Consumers in Ethiopia. *Chemosphere* **2016**, *162*, 252−260.
(57) Gunasekara, A. S.; Truong, T.; Goh, K. S.; Spurlock, F.; Tjeerdema, R. S. Environmental Fate and Toxicology of Fipronil. *J. Pestic. Sci.* **2007**, *32* (3), 189−199.
(58) Kucherenko, I. S.; Sanborn, D.; Chen, B.; Garland, N.; Serhan, M.; Forzani, E.; Gomes, C.; Claussen, J. C. Ion-Selective Sensors Based on Laser-Induced Graphene for Evaluating Human Hydration Levels Using Urine Samples. *Adv. Mater. Technol.* **2020**, *5* (6), 1901037.
(59) Li, Y.; Luong, D. X.; Zhang, J.; Tarkunde, Y. R.; Kittrell, C.; Sargunaraj, F.; Ji, Y.; Arnusch, C. J.; Tour, J. M. Laser-Induced Graphene in Controlled Atmospheres: From Superhydrophilic to Superhydrophobic Surfaces. *Adv. Mater.* **2017**, *29* (27), 1700496.
(60) Luong, D. X.; Yang, K.; Yoon, J.; Singh, S. P.; Wang, T.; Arnusch, C. J.; Tour, J. M. Laser-Induced Graphene Composites as Multifunctional Surfaces. *ACS Nano* **2019**, *13*, 2579−2586.
(61) Nasser, J.; Lin, J.; Zhang, L.; Sodano, H. A. Laser Induced Graphene Printing of Spatially Controlled Super-Hydrophobic/Hydrophilic Surfaces. *Carbon* **2020**, *162*, 570−578.
(62) Duy, L. X.; Peng, Z.; Li, Y.; Zhang, J.; Ji, Y.; Tour, J. M. Laser-Induced Graphene Fibers. *Carbon* **2018**, *126*, 472−479.
(63) Gao, L.; McCarthy, T. J. Contact Angle Hysteresis Explained. *Langmuir* **2006**, *22* (14), 6234−6237.
(64) Wenzel, R. N. Resistance of Solid Surfaces to Wetting by Water. *Ind. Eng. Chem.* **1936**, *28* (8), 988−994.
(65) Cassie, A. B. D.; Baxter, S. Wettability of Porous Surfaces. *Trans. Faraday Soc.* **1944**, *40* (0), 546.
(66) Nayak, P.; Kurra, N.; Xia, C.; Alshareef, H. N. Highly Efficient Laser Scribed Graphene Electrodes for On-Chip Electrochemical Sensing Applications. *Adv. Electron. Mater.* **2016**, *2* (10), 1600185.
(67) Liu, S.; Peng, Y.; Chen, J.; Shi, W.; Yan, T.; Li, B.; Zhang, Y.; Li, J. Engineering Surface Functional Groups on Mesoporous Silica: Towards a Humidity-Resistant Hydrophobic Adsorbent. *J. Mater. Chem. A* **2018**, *6* (28), 13769−13777.
(68) Law, K.-Y. Y. Definitions for Hydrophilicity, Hydrophobicity, and Superhydrophobicity: Getting the Basics Right. *J. Phys. Chem. Lett.* **2014**, *5* (4), 686−688.
(69) Garland, N. T.; McLamore, E. S.; Cavallaro, N. D.; Mendivelso-Perez, D.; Smith, E. A.; Jing, D.; Claussen, J. C. Flexible Laser-Induced Graphene for Nitrogen Sensing in Soil. *ACS Appl. Mater. Interfaces* **2018**, *10* (45), 39124−39133.
(70) Deng, H.; Zhang, C.; Xie, Y.; Tumlin, T.; Giri, L.; Karna, S. P.; Lin, J. Laser Induced MoS 2 /Carbon Hybrids for Hydrogen Evolution Reaction Catalysts. *J. Mater. Chem. A* **2016**, *4* (18), 6824−6830.
(71) Zhang, J.; Ren, M.; Li, Y.; Tour, J. M. *In Situ* Synthesis of Efficient Water Oxidation Catalysts in Laser-Induced Graphene. *ACS Energy Lett.* **2018**, *3* (3), 677−683.
(72) Ren, M.; Zhang, J.; Tour, J. M. Laser-Induced Graphene Synthesis of Co3O4 in Graphene for Oxygen Electrocatalysis and Metal-Air Batteries. *Carbon* **2018**, *139*, 880−887.
(73) Yang, Y.; Song, Y.; Bo, X.; Min, J.; Pak, O. S.; Zhu, L.; Wang, M.; Tu, J.; Kogan, A.; Zhang, H.; Hsiai, T. K.; Li, Z.; Gao, W. A Laser-Engraved Wearable Sensor for Sensitive Detection of Uric Acid and Tyrosine in Sweat. *Nat. Biotechnol.* **2020**, *38*, 217−224.
(74) Veder, J. P.; De Marco, R.; Clarke, G.; Chester, R.; Nelson, A.; Prince, K.; Pretsch, E.; Bakker, E. Elimination of Undesirable Water Layers in Solid-Contact Polymeric Ion-Selective Electrodes. *Anal. Chem.* **2008**, *80* (17), 6731−6740.
(75) Hu, J.; Stein, A.; Bühlmann, P. Rational Design of All-Solid-State Ion-Selective Electrodes and Reference Electrodes. *TrAC, Trends Anal. Chem.* **2016**, *76*, 102−114.
(76) Hu, J.; Ho, K. T.; Zou, X. U.; Smyrl, W. H.; Stein, A.; Buhlmann, P. All-Solid-State Reference Electrodes Based on Colloid-Imprinted Mesoporous Carbon and Their Application in Disposable Paper-Based Potentiometric Sensing Devices. *Anal. Chem.* **2015**, *87*, 2981.
(77) Guinovart, T.; Crespo, G. A.; Rius, F. X.; Andrade, F. J. A Reference Electrode Based on Polyvinyl Butyral (PVB) Polymer for Decentralized Chemical Measurements. *Anal. Chim. Acta* **2014**, *821*, 72−80.
(78) Bakker, E.; Pretsch, E. E.; Bühlmann, P. Selectivity of Potentiometric Ion Sensors. *Anal. Chem.* **2000**, *72* (6), 1127−1133.
(79) Li, F.; Ye, J.; Zhou, M.; Gan, S.; Zhang, Q.; Han, D.; Niu, L. All-Solid-State Potassium-Selective Electrode Using Graphene as the Solid Contact. *Analyst* **2012**, *137* (3), 618−623.
(80) Hu, J.; Stein, A.; Bühlmann, P. A Disposable Planar Paper-Based Potentiometric Ion-Sensing Platform. *Angew. Chem., Int. Ed.* **2016**, *55* (26), 7544−7547.
(81) Piek, M.; Piech, R.; Paczosa-Bator, B. All-Solid-State Nitrate Selective Electrode with Graphene/Tetrathiafulvalene Nanocomposite as High Redox and Double Layer Capacitance Solid Contact. *Electrochim. Acta* **2016**, *210*, 407−414.
(82) Rubinova, N.; Chumbimuni-Torres, K.; Bakker, E. Solid-Contact Potentiometric Polymer Membrane Microelectrodes for the Detection of Silver Ions at the Femtomole Level. *Sens. Actuators, B* **2007**, *121* (1), 135−141.
(83) Parate, K.; Rangnekar, S. V.; Jing, D.; Mendivelso-Perez, D. L.; Ding, S.; Secor, E. B.; Smith, E. A.; Hostetter, J. M.; Hersam, M. C.; Claussen, J. C. Aerosol-Jet-Printed Graphene Immunosensor for Label-Free Cytokine Monitoring in Serum. *ACS Appl. Mater. Interfaces* **2020**, *12*, 8592.
(84) Ye, R.; James, D. K.; Tour, J. M. Laser-Induced Graphene: From Discovery to Translation. *Adv. Mater.* **2019**, *31* (1), 1803621.
(85) Zhao, F.; He, J.; Li, X.; Bai, Y.; Ying, Y.; Ping, J. Smart Plant-Wearable Biosensor for *In-Situ* Pesticide Analysis. *Biosens. Bioelectron.* **2020**, *170* (June), 112636.
(86) Govindasamy, M.; Mani, V.; Chen, S. M.; Chen, T. W.; Sundramoorthy, A. K. Methyl Parathion Detection in Vegetables and Fruits Using Silver@Graphene Nanoribbons Nanocomposite Modified Screen Printed Electrode. *Sci. Rep.* **2017**, *7* (1), 1−11.
(87) Sakthinathan, S.; Kubendhiran, S.; Chen, S. M.; Karuppiah, C.; Chiu, T. W. Novel Bifunctional Electrocatalyst for ORR Activity and Methyl Parathion Detection Based on Reduced Graphene Oxide/Palladium Tetraphenylporphyrin Nanocomposite. *J. Phys. Chem. C* **2017**, *121* (26), 14096−14107.
(88) Mehta, J.; Vinayak, P.; Tuteja, S. K.; Chhabra, V. A.; Bhardwaj, N.; Paul, A. K.; Kim, K. H.; Deep, A. Graphene Modified Screen Printed Immunosensor for Highly Sensitive Detection of Parathion. *Biosens. Bioelectron.* **2016**, *83*, 339−346.
(89) Kesik, M.; Ekiz Kanik, F.; Turan, J.; Kolb, M.; Timur, S.; Bahadir, M.; Toppare, L. An Acetylcholinesterase Biosensor Based on a Conducting Polymer Using Multiwalled Carbon Nanotubes for Amperometric Detection of Organophosphorous Pesticides. *Sens. Actuators, B* **2014**, *205*, 39−49.
(90) Hondred, J. A.; Johnson, Z. T.; Claussen, J. C. Nanoporous Gold Peel-and-Stick Biosensors Created with Etching Inkjet Maskless Lithography for Electrochemical Pesticide Monitoring with Microfluidics. *J. Mater. Chem. C* **2020**, *8* (33), 11376−11388.

https://doi.org/10.1021/acsnano.1c04197
ACS Nano 2022, 16, 15−28

(91) Hondred, J. A.; Medintz, I. L.; Claussen, J. C. Enhanced Electrochemical Biosensor and Supercapacitor with 3D Porous Architectured Graphene *via* Salt Impregnated Inkjet Maskless Lithography. *Nanoscale Horizons* **2019**, *4* (3), 735−746.
(92) Nelis, J. L. D.; Tsagkaris, A. S.; Zhao, Y.; Lou-Franco, J.; Nolan, P.; Zhou, H.; Cao, C.; Rafferty, K.; Hajslova, J.; Elliott, C. T.; Campbell, K. The End User Sensor Tree: An End-User Friendly Sensor Database. *Biosens. Bioelectron.* **2019**, *130*, 245−253.
(93) Chen, B.; Jiang, Y.; Tang, X.; Pan, Y.; Hu, S. Fully Packaged Carbon Nanotube Supercapacitors by Direct Ink Writing on Flexible Substrates. *ACS Appl. Mater. Interfaces* **2017**, *9* (34), 28433−28440.
(94) Peng, Z.; Lin, J.; Ye, R.; Samuel, E. L. G.; Tour, J. M. Flexible and Stackable Laser-Induced Graphene Supercapacitors. *ACS Appl. Mater. Interfaces* **2015**, *7* (5), 3414−3419.
(95) Zhou, H.; Peng, Y.; Wu, H. B.; Sun, F.; Yu, H.; Liu, F.; Xu, Q.; Lu, Y. Fluorine-Rich Nanoporous Carbon with Enhanced Surface Affinity in Organic Electrolyte for High-Performance Supercapacitors. *Nano Energy* **2016**, *21*, 80−89.
(96) Joon, N. K.; He, N.; Ruzgas, T.; Bobacka, J.; Lisak, G. PVC-Based Ion-Selective Electrodes with a Silicone Rubber Outer Coating with Improved Analytical Performance. *Anal. Chem.* **2019**, *91* (16), 10524−10531.
(97) Liu, H.; Gao, J.; Xue, M.; Zhu, N.; Zhang, M.; Cao, T. Processing of Graphene for Electrochemical Application: Non-covalently Functionalize Graphene Sheets with Water-Soluble Electroactive Methylene Green. *Langmuir* **2009**, *25*, 12006.
(98) Baptista-Pires, L.; Pérez-López, B.; Mayorga-Martinez, C. C.; Morales-Narváez, E.; Domingo, N.; Esplandiu, M. J.; Alzina, F.; Torres, C. M. S.; Merkoçi, A. Electrocatalytic Tuning of Biosensing Response through Electrostatic or Hydrophobic Enzyme-Graphene Oxide Interactions. *Biosens. Bioelectron.* **2014**, *61*, 655.
(99) Akkarachanchainon, N.; Rattanawaleedirojn, P.; Chailapakul, O.; Rodthongkum, N. Hydrophilic Graphene Surface Prepared by Electrochemically Reduced Micellar Graphene Oxide as a Platform for Electrochemical Sensor. *Talanta* **2017**, *165*, 692.
(100) Feng, J.; Guo, Z. Wettability of Graphene: From Influencing Factors and Reversible Conversions to Potential Applications. *Nanoscale Horizons* **2019**, *4* (2), 339−364.
(101) Moeremans, B.; Cheng, H.-W.; Hu, Q.; Garces, H. F.; Padture, N. P.; Renner, F. U.; Valtiner, M. Lithium-Ion Battery Electrolyte Mobility at Nano-Confined Graphene Interfaces. *Nat. Commun.* **2016**, *7* (1), 12693.
(102) Sheng, Y.; Fell, C. R.; Son, Y. K.; Metz, B. M.; Jiang, J.; Church, B. C. Effect of Calendering on Electrode Wettability in Lithium-Ion Batteries. *Front. Energy Res.* **2014**, *2* (DEC), 56.
(103) Papadopoulou, E.; Megaridis, C. M.; Walther, J. H.; Koumoutsakos, P. Ultrafast Propulsion of Water Nanodroplets on Patterned Graphene. *ACS Nano* **2019**, *13* (5), 5465−5472.
(104) Preston, D. J.; Mafra, D. L.; Miljkovic, N.; Kong, J.; Wang, E. N. Scalable Graphene Coatings for Enhanced Condensation Heat Transfer. *Nano Lett.* **2015**, *15* (5), 2902−2909.
(105) Rafiee, J.; Mi, X.; Gullapalli, H.; Thomas, A. V.; Yavari, F.; Shi, Y.; Ajayan, P. M.; Koratkar, N. A. Wetting Transparency of Graphene. *Nat. Mater.* **2012**, *11* (3), 217−222.
(106) Cohen-Tanugi, D.; Grossman, J. C. Water Desalination across Nanoporous Graphene. *Nano Lett.* **2012**, *12* (7), 3602−3608.
(107) You, Y.; Sahajwalla, V.; Yoshimura, M.; Joshi, R. K. Graphene and Graphene Oxide for Desalination. *Nanoscale* **2016**, *8*, 117−119.
(108) Homaeigohar, S.; Elbahri, M. Graphene Membranes for Water Desalination. *NPG Asia Mater.* **2017**, *9* (8), e427−e427.
(109) Ding, G.; Jiao, W.; Chen, L.; Yan, M.; Hao, L.; Wang, R. A Self-Sensing, Superhydrophobic, Heterogeneous Graphene Network with Controllable Adhesion Behavior. *J. Mater. Chem. A* **2018**, *6* (35), 16992−17000.
(110) Zhang, Q.; Xu, X.; Li, H.; Xiong, G.; Hu, H.; Fisher, T. S. Mechanically Robust Honeycomb Graphene Aerogel Multifunctional Polymer Composites. *Carbon* **2015**, *93*, 659.
(111) Akhtar, N.; Anemone, G.; Farias, D.; Holst, B. Fluorinated Graphene Provides Long Lasting Ice Inhibition in High Humidity. *Carbon* **2019**, *141*, 451.
(112) Umezawa, Y.; Bühlmann, P.; Umezawa, K.; Tohda, K.; Amemiya, S. Potentiometric Selectivity Coefficients of Ion-Selective Electrodes. Part I. Inorganic Cations (Technical Report). *Pure Appl. Chem.* **2000**, *72* (10), 1851−2082.

https://doi.org/10.1021/acsnano.1c04197
ACS Nano 2022, 16, 15−28